

# Track Anything Behind Everything: Zero-Shot Amodal Video Object Segmentation

Finlay G. C. Hudson  
Department of Computer Science  
University of York  
York, United Kingdom  
fgch500@york.ac.uk

William A. P. Smith  
Department of Computer Science  
University of York  
York, United Kingdom  
william.smith@york.ac.uk



Figure 1. Given an input video (top) and a prompt (e.g. point clicks) to define a query mask (top, white) we track segmentation masks of the visible regions (*modal* masks) using a video object segmentation method such as SAM 2 [36] (top, red). We propose to use a fine-tuned generative video diffusion model to outpaint the occluded object (middle) providing zero-shot, amodal video object segmentation (bottom).

## Abstract

We present *Track Anything Behind Everything (TABE)*, a novel dataset, pipeline, and evaluation framework for zero-shot amodal completion from visible masks. Unlike existing methods that require pretrained class labels, our approach uses a single query mask from the first frame where the object is visible, enabling flexible, zero-shot inference. Our dataset, *TABE-51* provides highly accurate ground truth amodal segmentation masks without the need for human estimation or 3D reconstruction. Our *TABE* pipeline is specifically designed to handle amodal completion, even in scenarios where objects are completely occluded. We also introduce a specialised evaluation framework that isolates amodal completion performance, free from the influence of traditional visual segmentation metrics. Dataset, model and code will be made available.

## 1. Introduction

Humans have an understanding of an object beyond just the visible regions that can be observed. This stems from our strong notion of *object permanence* [1] – the concept that objects maintain their identity and continuity over time, regardless of visibility. Humans also have a notion of how objects deform or respond to other elements of an environment, allowing our minds eye to still be able to predict where an object exists, even when occluded. This concept is called *amodal completion* [2, 30] and is the focus of this paper.

Recent advances in computer vision have significantly improved the ability to determine an object’s location within a scene based solely on its visible pixels. Methods like SAM2 [36], DINOv2 [32], and Mask2Former [8] now produce segmentation masks with a level of quality and accuracy that would have seemed out of reach just a few years

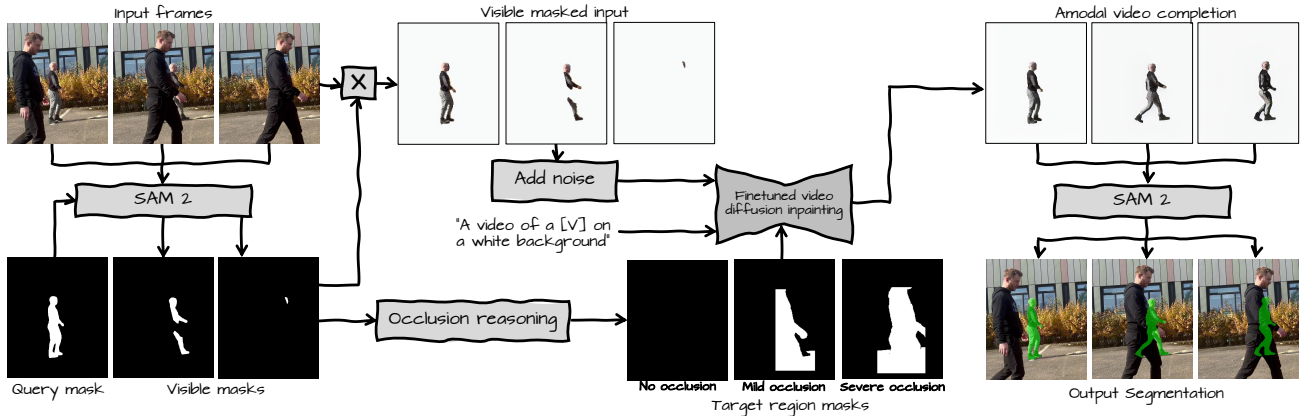


Figure 2. Overview of our TABE pipeline. This figure demonstrates how input frames from a video, combined with a single query mask, are processed to produce high-quality, amodal completion segmentation masks

ago. On the other hand, a model’s ability to perceive and predict the position of objects obscured by occlusions has not advanced as rapidly [24, 60]. Two primary challenges underlie this gap. First, is that getting real-world ground truth data for objects behind occlusions is an extremely difficult and resource intensive task [48]. Second, defining “ground truth” itself is complex for occluded objects [54], as human perception of these hidden elements often involves educated guesses based on context, motion, or the object’s anticipated behaviour. For example, if a cup obscures a ball on a table at eye level, it is ambiguous whether the ball has been fully contained by the cup or simply hidden behind it. Until the cup moves, this information remains uncertain, and even if the ball doesn’t reappear, one might assume it was concealed rather than removed. This ambiguity in visual perception highlights a core problem for machine learning models. Humans can constantly update their understanding based on context and new information [21], while models lack this adaptive intuition [41]. Indeed, this phenomenon is leveraged in magic tricks, where the brain’s assumptions can make it susceptible to deception.

The importance of machine learning models being able to understand object permanence, particularly through amodal completion, lies in their ability to function in a manner more aligned with human cognition. Infants begin to develop a basic level of object permanence around the age of 3.5 months and continue refining this ability until about 14 months, by which point most tasks involving object permanence can be successfully solved [29]. This developmental milestone highlights how deeply ingrained the concept of object permanence is in human cognition, providing a valuable framework for developing more intuitive and human-like machine learning models.

When considering specific use cases for this to solve, a compelling application could be tracking objects in complex environments. Currently, many trackers employ re-identification methodologies [4, 56, 57, 59] to maintain ob-

ject tracking through occlusions. However these can often be complex and non-robust [31]. By incorporating amodal completion in video, we could instead leverage a human-like ability to continuously reference an object’s position, even when it is behind occluders, enabling uninterrupted tracking. This approach is crucial for tasks such as autonomous driving [7]. Furthermore, amodal completion has been shown to improve object recognition, as the ability to complete objects amodally can support accurate class recognition [33].

We introduce a dataset with evaluation metrics which are able to isolate and evaluate a model’s ability to complete the task of amodal completion, we will also introduce a novel pipeline to solve this challenge, illustrated in Fig 2.

## 2. Related Work

**Amodal Completion** Amodal completion in computer vision refers to the task of inferring the parts of an object that are occluded or missing in a given image or video frame. This involves reconstructing the complete shape or structure of an object, even when parts of it are hidden by other objects or the environment. Unlike traditional segmentation, which focuses on visible parts of an object, amodal completion aims to predict the complete, unseen regions based on contextual information and the object’s known properties. The approach to solving amodal completion can be categorized into two main strategies.

*Amodal Instance Segmentation* involves training a model to be able to segment both visible and non-visible portions of an object [13, 18, 20, 22, 25, 28, 47, 51, 53]. This type of approach requires all test objects to be of classes that were seen during training time, meaning that these methods cannot be translated to a zero-shot paradigm.

Within the *Amodal Completion from a Visible Mask* paradigm, a model must be able to amodally complete any object based on its visible mask and frame information

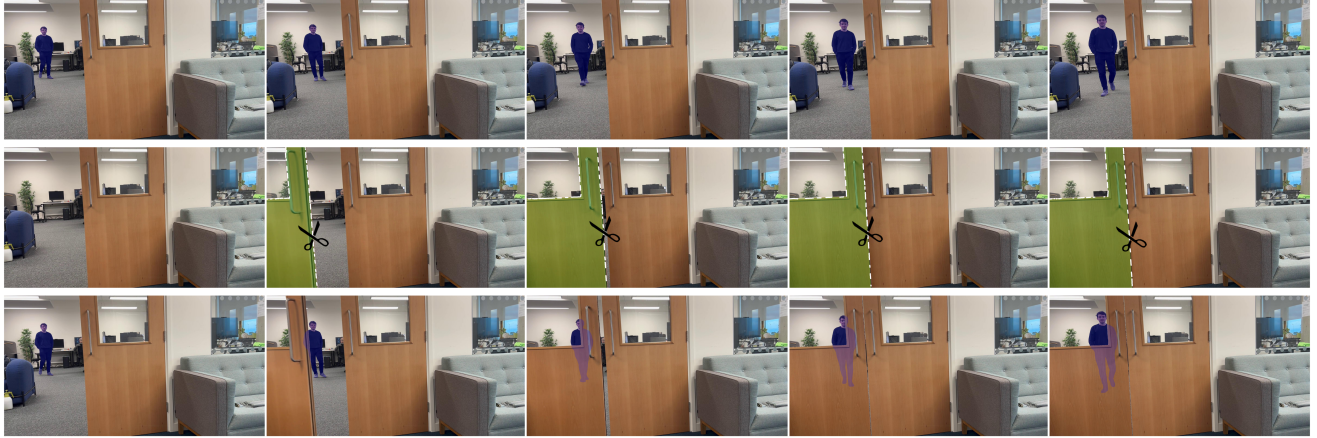


Figure 3. An overview of our dataset curation approach: from a static camera we observe two different scenes, shown in the top and middle row. We then extract the door from the middle scene and composite it onto the top scene, creating a realistic test scene (bottom row) while maintaining a ground truth accurate amodal segmentation mask.

[33, 54]. Although this method relies on extra data being provided, either as ground truth or from a modal instance segmentation model [8, 23, 32, 36], it allows for zero-shot amodal completion.

**Video Amodal Completion** Temporal cues play a crucial role in human ability to amodally complete objects, significantly reducing the ambiguity that often arises from partial occlusions. This skill develops early in life, with infants using spatiotemporal continuity to understand that objects persist and remain cohesive even when partially out of view [43]. Amodal completion from visible masks can be extended for entire video sequences, as only the visible mask of the object in the first frame is required. This initial mask can be generated either through a segmentation method such as SAM2 [36], based on point clicks for quick object localisation, or directly from ground-truth data if available [48]. Image-based amodal techniques [33, 54] fail to leverage temporal cues and thus struggle with amodal completion in the presence of severe occlusion. These methods also use priors that come from images without severe occlusion, one such prior is pix2gestalt [33] using CLIP [35] embeddings for the whole image to provide context for the inpainting. This is not necessarily helpful if the occluding objects or background scene do not relate strongly to the occluded object. Similar to our approach, pix2gestalt leverages partially observed, unoccluded areas as input for an outpainting process. However, we have developed a novel pipeline specifically designed for video tasks to address the issues outlined above. In our method, we use unoccluded frames as reference points to fine-tune our generative model. Additionally, we introduce a target region mask, derived from depth data and interpolated bounding box information, to restrict the areas where the model can inpaint.

**Video Diffusion** Video diffusion methods are a subset of generative models designed to generate high-quality video

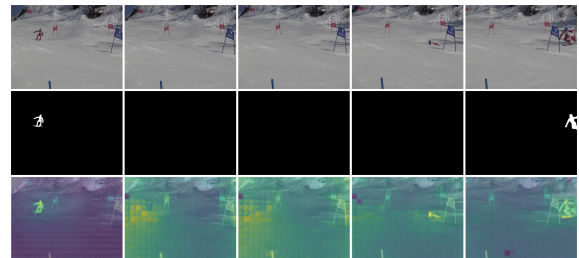


Figure 4. Issue with TCOW [48] metrics for amodal completion - the top row shows the input frames, whilst the middle row shows the query mask (left box) and target mask (right box). The bottom row presents the model's output heatmaps, highlighting that evaluating the model solely against the target masks overlooks the non-visible pixels that are missed in previous frames.

sequences by leveraging diffusion processes, which are originally popular in image generation tasks [38, 40, 55]. Video diffusion extends the capabilities of the image-based diffusion to handle temporal consistency across frames. Allowing for coherent videos to be generated [16]. Video diffusion models can be conditioned in various ways, ranging from an input image [5] to a full text description [16]. For this task we need to ensure the video diffusion model can be conditioned by both an image and inpainting region. The COCOCO [62] methodology is a perfect fit for this purpose, taking both an image and inpainting region as input as well as employing global attention mechanisms to capture motion over time. This approach enables the generation of lifelike and consistent motion for query objects based on the visible mask information. Furthermore, video diffusions methods are trained on large and diverse datasets, such as WebVid-10M [3], resulting in highly generalised models that are well-suited for the zero-shot paradigm we are working within.

**Dataset** Formulating a dataset to test amodal completion

with pixel-level annotations in videos presents significant challenges due to the complexities of annotating pixels that are not visible. Computer-generated synthetic data enables lifelike objects or shapes to be placed within a scene and manipulated by using motion tools [14, 15, 42, 46, 53], physics modelling [20, 37, 48], or simply occluded at an image level [10–12]. This allows for object to interact, generating complex scenarios while ensuring complete control over interactions and occlusions. By using synthetic objects, each object’s pixel-level location within the scene can be perfectly tracked, even when occluded, thus providing comprehensive ground truth data for amodal completion tasks. However, synthetic datasets contribute to the sim2real gap [17, 50], where even highly sophisticated, physics-based modelling fails to fully replicate the complexities of real-world data. TCOW’s [48] demonstrates this challenge well. Their Kubric dataset, which offers visually realistic and detailed object interactions, supports excellent model performance within synthetic test sets. Yet, when evaluated on real-world data, the model’s performance drops significantly - emphasising that even high quality synthetic data cannot capture the complexities and diversity of real-world situations [27]. Given the limitations of synthetic data for developing models suited to real-world applications, many datasets focus on real-world data-driven techniques for amodal segmentation. The most straightforward method for this is to have a human simply annotate their estimation of an object’s amodal segmentation [13, 34, 61], however, while intuitive, this method relies on human estimation which can be incorrect leading to possible inaccurate ground truth data. Additionally, it is extremely time and labour intensive, restricting its scalability, especially for images with extensive or complex occlusions. Consequently, these datasets are often limited to scenes with simpler occlusions, as objects with significant occlusion would require even more careful estimation as well as likely some temporal information. One method to generate fairly accurate ground truth annotations for occluded objects is to leverage 3D data [26, 54]. By capturing an object from multiple viewpoints, this method allows for a more comprehensive inference of the object’s shape and provides a reliable mask, even through areas of occlusion. However, this method has its limitations: 3D data acquisition is both expensive and resource-intensive, requiring specialised equipment and precise control over the scene to reproject the amodal mask accurately into a specific camera perspective. Furthermore, the accuracy of this approach relies heavily on the quality of the generated 3D mesh, which often requires manual refinement and filtering. Consequently, the scalability and feasibility of this approach in less controlled environments remain restricted. Finally, another approach to dataset collection blends synthetic and real-world methods through compositing real im-

ages. This technique places an object, cut from one scene, onto a natural background where it appears unoccluded. It has shown success in several other domains, including image classification [49], image detection [6, 9], GAN’s [58] and visible image segmentation [23]. In amodal segmentation, pix2gestalt’s [33] training strategy employs this cut-and-paste compositing approach. However, as with similar techniques, objects in video diffusion models are often placed randomly, resulting in unrealistic occlusions that create a realism gap when applied to real-world scenarios, particularly in video data.

### 3. Task

The *zero-shot amodal video segmentation* (ZS-AVS) task is defined as follows. We are given as input a  $T$ -frame video  $\mathbf{x} \in \mathbb{R}^{T \times H \times W \times 3}$  along with a prompt of some form (e.g. text or point clicks) used to define the object of interest in some reference frame (assumed to be frame 1). The prompt is used to compute the binary query mask  $\mathbf{m}_q \in \{0, 1\}^{H \times W}$  which segments the object of interest in the reference frame. It is assumed that the object is completely unoccluded in the reference frame. The goal is to learn a function  $f$  that estimates amodal segmentation masks for the tracked object in every frame:

$$\mathbf{m}_o = f(\mathbf{x}, \mathbf{m}_q), \quad (1)$$

where  $\mathbf{m}_o \in \{0, 1\}^{T \times H \times W}$  is the binary object mask in every frame. This must delineate the object even behind occluders and even when none of the object is visible based on information from surrounding frames and the context of the object itself.

**TABE-51** Current approaches to video-specific amodal segmentation are primarily limited to synthetic data-based methods [14, 20, 46, 48, 53] or rely on bounding box annotations [18]. To address this, we present TABE-51 (Track Anything Behind Everything 51), a video amodal segmentation dataset that provides high-quality ground truth labels for occluded objects, eliminating the need for human assumptions about hidden pixels. TABE-51 leverages a compositing approach using real-world video clips: we record an initial clip of an object without occlusion and then overlay a second clip featuring the occluding object. This compositing yields realistic video sequences with natural motion and highly accurate ground truth masks, allowing models to be evaluated on how well they handle occluded objects in authentic scenarios.

This dataset setup contrasts with existing methods like TCOW [48], which evaluates performance only on visible object pixels in real-world settings. As illustrated in Fig 4, methods like TCOW struggle to locate the skier when occluded by the hill; metrics are computed based on the visible frames only, where the skier reappears. By testing only on unoccluded regions, TCOW does not fully

	Scenes	Images	Occluded Frames	Heavily Occluded Frames	Fully Occluded Frames
<b>TABE-51</b>	51	2163	1093	556	30

Table 1. TABE-51 dataset metrics. Heavily occluded frames are defined as frames with  $>50\%$  occlusion, while fully occluded is defined as when the object is fully non-visible.

	Rubric Office	Rubric Cup Games	Rubric DAV/YTB
TCOW	69.4	38.3	52.8
SAM2	<b>72.7</b>	<b>55.8</b>	<b>68.9</b>

Table 2. Comparison of TCOW [48] and SAM2 [36] based on average IoU metrics on different datasets. This table demonstrates that TCOW’s metrics are inadequate for assessing amodal completion, as SAM2—despite operating solely on visible pixels—outperforms TCOW in these evaluations

assess model understanding of occlusions. Consequently, visible-pixel segmentation methods, such as SAM2 [36], can achieve high scores on TCOW’s test set even without handling occlusions accurately, as shown in Fig 2. In contrast, TABE-51 provides a robust benchmark for evaluating how well segmentation methods track and predict occluded objects throughout the entire video sequence. Further, TABE-51 enables a evaluation of amodal completion methods in challenging scenarios where an object has few or even no visible pixels in certain frames. This dataset pushes models to utilise temporal information to infer the occluded object’s location and shape based on surrounding frames. Such scenarios highlight limitations in existing methods like pix2gestalt [33], which may struggle in video settings where tracking through heavy occlusions is necessary. Fig 5 highlights one such failure case. This benchmark ensures models are aiming to handle real-world occlusions effectively. Dataset statistics for TABE-51 are shown in 1

**Evaluation Metrics** We evaluate model performance using average Intersection over Union (IoU) between a model’s output and the corresponding ground truth amodal mask. However, to further test a methodologies ability to accurately amodally complete objects through occlusions we test specifically in three challenging scenarios:

- *Occlusion IoU* - this is calculated on frames with any form of occlusion.
- *Full Occlusion IoU* - this is calculated on frames whereby there are no visible pixels of the object.
- *Non Visible Pixel IoU* - this metric is to attempt to assert how good the model is specifically on occluded pixels. We assess this by removing any ground truth visual pixels from the prediction mask and ground truth mask and only calculate IOU between these non visible pixels.

This evaluation approach, alongside our amodally accurate ground-truth dataset, allows us to assess a model’s ability to generate amodally complete segmentation masks for oc-



Figure 5. Pix2gestalt [33] cannot amodally complete with very little information. The left image showcases the frame of interest, the center image shows this frame with visible pixels labelled (green) and the ground truth amodal mask (blue), while the right image shows the frame with pix2gestalt’s prediction mask (red).

cluded objects. By focusing on amodal completion, we ensure the model is tested on its capacity to infer the full shape of occluded objects. Separating it from methods that just segment visible pixels, which we view as a different task.

## 4. Overview

We propose a novel zero-shot amodal video object segmentation method, as shown in Figure 2. We call this methodology TABE (Track Anything Behind Everything). The key idea is to apply outpainting to the visible regions of the tracked object using a video diffusion model.

From an input video and prompts to describe the target object in frame 1 (we use point clicks but this could also be natural language description), we use a zero-shot segmentation model to find the *query mask*. We provide this query mask and the video frames to a visible VOS method (SAM 2 [36]) to compute the *visible masks* for each frame (which might be empty if the object is completely occluded). We use these to produce the *visible masked input* providing images containing only the object itself, deforming over time and with missing parts caused by occlusions. It is to these images that we apply our video diffusion outpainting method (described in Section 5), prompting the model to create a video of only the object on a white background. This provides *amodal video completion* output frames. Since sometimes the outpainting process reintroduces some background elements or other artefacts, we re-run VOS (SAM 2 [36]) on these frames with the original query mask, providing the final segmentation result.

We found that video diffusion outpainting was liable to produce additional spurious content without restricting the region in which to outpaint (for example, if the object being tracked was a person, the outpainting result might hallucinate an additional second person). In addition, during the finetuning process for the video diffusion model, we need per-frame labels indicating which frames contain occlusion. In order to tackle both of these problems we perform *occlusion reasoning* prior to video diffusion (see Fig 6).

**Target region masks** We restrict the diffusion outpainting to a *target region mask* per frame. These masks combine two cues to label likely areas the object could cover. First, we use monodepth (Depth Anything v2 [52]) to esti-

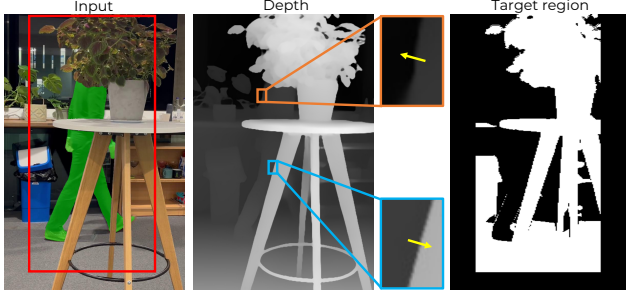


Figure 6. Occlusion reasoning. From an input frame (left), visible region mask (green) and approximate bounding box (red) we detect occluded frames and create target region masks for outpainting. From an estimated depth map (middle), boundary points where the derivative of depth in the direction outward facing normal (yellow) is negative (orange) are unlikely to be occlusion boundaries but where it is positive (blue) it is a likely occlusion. The target region mask comprises pixels inside the bounding box with depth less than the mask region.

mate a depth map. We compare pixel depth values against the mean depth inside the visible region mask. Any pixel with a depth value smaller than this mean is a candidate for outpainting. Second, we further restrict this candidate set of pixels by requiring that they lie within an approximate amodal bounding box. We estimate these bounding boxes using temporal continuity. We initialise the bounding boxes conservatively using the visible region masks. For frames with no visible pixels, we linearly interpolate or extrapolate from adjacent frames. If the change in bounding box area indicates a potential occlusion, we test the occlusion labels on the visible mask region boundary (see below) and grow the bounding box by assuming its area should remain the same.

**Occlusion labelling** Intuitively, at points on the boundary of the visible mask region where the estimated depth is larger just outside the mask compared to inside, this is likely to be the true boundary of the object as opposed to an occlusion boundary. On the other hand, where the depth is smaller, it is likely that the object continues behind this closer object and so this is an occlusion boundary. Using the visible mask and estimated depth, we compute an occlusion measure which is the proportion of the boundary believed to be an occlusion boundary. Suppose that the visible mask region for a frame is defined by the set of pixels belonging to the mask  $S \subset \{1, \dots, W\} \times \{1, \dots, H\}$ , with boundary  $\partial S$ . First, we define an indicator function for a point on the boundary  $(u, v)$  with outward facing normal  $\vec{n}(u, v)$ :

$$g(u, v) = \begin{cases} 1 & \nabla z(u, v) \cdot \vec{n}(u, v) > t \\ 0 & \text{otherwise} \end{cases}, \quad (2)$$

where  $z(u, v)$  is the estimated depth at position  $(u, v)$  and  $\nabla z(u, v) \cdot \vec{n}(u, v)$  is the directional derivative of the depth function in the direction of the outward facing normal to the

boundary. This quantity is positive at potential occlusion boundary points and we use a  $t$  slightly larger than 0 for robustness to noise. Then we compute  $f_{\text{occ}}(S) \in [0, 1]$ , the proportion of the boundary that is potential occlusion as:

$$f_{\text{occ}}(S) = \frac{\int_{(u,v) \in \partial S} g(u, v) ds}{\int_{(u,v) \in \partial S} ds}, \quad (3)$$

and  $ds$  represents the differential arc length along the boundary to the visible mask  $\partial S$ . Finally, we label frame  $i$  as unoccluded ( $V_i = 1$ ) if  $f_{\text{occ}}(S)$  is below a threshold, occluded if  $f_{\text{occ}}(S)$  is above a threshold or left the frame (as indicated by bounding box extrapolation), with  $V_i = 0$  for the final two cases.

## 5. Finetuned Diffusion Model

Our approach relies on outpainting a partially observed object using a video diffusion model. We found that using a generic outpainting model did not lead to good results as the model did not adhere to the constraints implied on the object and motion by the partial observations. For this reason, we propose a finetuning process in which the model is first specialised to the specific object we wish to outpaint.

**Baseline Model** We use the pretrained video diffusion model from COCO [62], which adapts Stable Diffusion Inpainting [38] for video sequences by incorporating a temporal UNet module [39]. This temporal UNet is specifically modified to enhance motion consistency across frames, thanks to improved global information capture. The method is trained on a huge and diverse image dataset, enabling them to retain the generalisation that was possible in the original Stable Diffusion Inpainting.

**Finetuning** We employ a similar finetuning strategy to that of Realfill [45] but adapt it to be able to work on video data rather than just images. As with Dreambooth [40], Realfill aims to finetune the stable diffusion model with just a few training images utilising Low Rank Adaptations (LoRA) [19] to add learnable residual modules to each weight in the network. This approach allows the primary model parameters to remain frozen, thus retaining the generalisation capability of the original diffusion model while adapting it to the new data. Further, as with Dreambooth, a fixed prompt containing a rare token is employed to specifically overfit the model to the object of interest. This allows the model to associate the token directly with the visual characteristics of that particular object. At inference time, we need the model to output an amodal completion of the object of interest with a white background, allowing the object to be easily isolated for amodal segmentation. We begin by isolating the pixels within an estimated visible mask of the target object, setting all other pixels in the frame to white. Then, inspired by [44], we generate random binary masks that serve two purposes. First, we ensure some

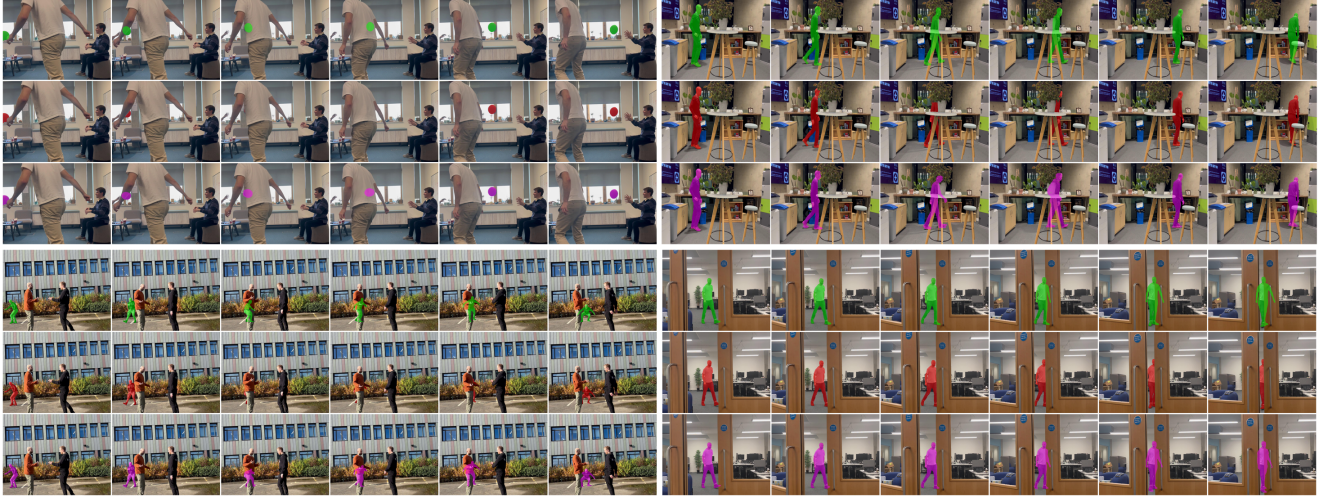


Figure 7. Examples of results on the TABE-51 dataset with our TABE method. In each video block, the top row’s green mask showcases the amodal ground truth, the second row’s red mask showcases the ground-truth visual pixels and the bottom row’s magenta masks show the predictions from the TABE method.

masks are generated that occlude parts of the object of interest. These partial occlusions encourage the model to learn how to recreate complete hidden portions of the object accurately, thus enhancing the model’s amodal completion ability. Second, additional masks are randomly applied to areas outside the object of interest. This teaches the model to generate a consistent white background in those regions. These constraints ensure the model does not fill in non-object areas whilst focusing its inpainting efforts solely on reconstructing the object. Finally, while we complete full sequences of frames at each training iteration, we only optimise losses from frames which we have labelled as unoccluded. This ensures that the model receives reliable training signal for those areas without introducing noise from undefined occluded regions. Concretely, we adapt the Realfill [45] loss as follows:

$$\mathcal{L} = \sum_{i=1}^T V_i \cdot \mathbb{E}_{x,t,\epsilon,m} \|\epsilon_{\theta}(x_t, t, p, m, (1-m) \odot x) - \epsilon\|_2^2, \quad (4)$$

where  $x$  is a block of frames,  $p$  is a fixed language prompt “A video of a [V] on a white background”,  $m$  is the randomly occluded mask,  $t$  is the diffusion time step and  $\epsilon$  the noise.  $V_i$  masks the loss for occluded frames where the target inpainting is not known.

Due to this being within the pipeline, as explained in Section 4, what we determine to be occluded versus unoccluded frames is not based on ground truth data — apart from the initial frame where no occlusion is assumed (as defined in Section 3). Therefore, the combination of a generalised pretrained model, diverse samples of the target object, and the use of random binary masks enables the model to learn a robust representation of the object, even without perfect occlusion labels for each frame.

Method	GT Vis Mask	GT Bbox	Occlusion IoU	Full Occlusion IoU	Non Visible Pixel IoU
pix2gestalt [33]	N	NA	0.447	0.007	0.222
TCOW [48]	N	NA	0.450	0.190	0.232
SDAmodal [54]	N	Y	0.508	0.032	0.202
TABE	N	N	<b>0.658</b>	<b>0.418</b>	<b>0.487</b>
TABE-ablation	N	Y	0.676	0.481	0.508
TABE-ablation	Y	N	0.675	0.495	0.503
TABE-ablation	Y	Y	0.692	0.496	0.523

Table 3. The results show the average IoU scores on the TABE-51 dataset. The top block of results are benchmark comparisons, while the bottom are ablation studies that examine different levels of ground truth inputs.

## 6. Experiments

In this section, we evaluate three model modalities for generating amodal segmentation masks, using the TABE-51 dataset as a benchmark. The evaluation metrics and ground-truth data from TABE-51, as outlined in Section 3, facilitate a comprehensive assessment of each model’s performance in amodal completion for occluded objects.

**Transformers** The first modality we compare against is a transformer approach, namely TCOW [48]. This architecture addresses a task closely aligned with the one in this paper, where the model takes video frames and a query mask as input. The method slightly differs by trying to also output masks of occluder or container objects, however they do also output masks for this query object at each frame, so this is what we will be using in these experiments. Although the authors themselves state that amodal completion is not “the main point” of the method, it still provides valuable outputs, and the model performs impressively in amodally completing masks, especially on synthetic datasets. For fairness in this evaluation, we extend the input to TCOW beyond the query mask by also providing the SAM2 visible mask out-

puts for each frame. This ensures a more comparable test scenario, as SAM2’s visible masks provide additional contextual information that could enhance the model’s performance during the evaluation. We use the pretrained weights provided with the model.

**Image Diffusion** As discussed in Section 3 the majority of data sources for amodal completion are images and hence most models created to solve amodal completion work on individual images rather than videos. We pick two state of the art image diffusion methods, using pretrained weights provided with each model. **pix2gestalt** [33]: This method takes in the visible mask of an image, the full image, as well as CLIP [35] embeddings of the full image. The output is the amodally reconstructed object, from which an amodal segmentation mask can be derived. This method showcases great results across a number of modalities including art and photographs. **SDAmodal** [54]: This method differs from those that rely solely on the outputs of image diffusion models. Instead they extract multi-scale features from an image diffusion model and combine these with features from a visual mask, which are then passed through decoding layers to produce the amodal segmentation mask. An intuitive methodology that removes the need for the extra mask extraction stage as in our method or pix2gestalt. This method relies on both visual mask and bounding box inputs. For the visual mask input, we utilise SAM2 outputs, while for the bounding box inputs, we provide ground truth amodal bounding boxes, doing so removes any potential inaccuracies that could arise from using our proprietary bounding box estimation, allowing the method to operate under optimal conditions and performance is not influenced by external factors.

**Video Methods** For this specific task, finding video models that align with our task paradigm proved difficult. Existing methods, such as those used in instance segmentation or bounding box prediction, are tailored to work within predefined categories or rely on prior knowledge of the objects in the video, making them unsuitable for zero-shot tasks. These models typically require labelled data or training on specific object categories [13, 18, 20, 25, 28, 47, 51, 53], rather than operating solely from a query image without any prior object-specific information. Hence, we use our TABE method to generate baseline results for the TABE-51 dataset presented in this paper.

**Results** We showcase evaluation results within Table 3. It showcases our TABE method out performing other methods by a significant margin on all metrics defined. Among the other methods TCOW performs best when an item is fully occluded, this is due to it being able to harness temporal information to assume the shape of an object when it is behind occlusion, this is something image diffusion techniques cannot do. Apart from this, all other method perform

in within a 6% range of each other, showcasing similar performance, although SDAmodal achieves the best results on frames whereby the object has any occlusion, highlighting how stable diffusion techniques are strong at getting amodal segmentation masks, even when they have no temporal information. Fig 7 showcases some outputs of our TABE method on the TABE-51 dataset, further to those already shown in other figures. These results demonstrate the high success rate of the TABE method, though in some cases, it slightly misjudges the specific pose of the object. We showcase further qualitative results from other public datasets as well as ablation studies and failure cases within the supplementary material section.

**TABE Ablation - GT vs Pred Inputs** In the bottom block of Table 3 we present different permutations of the level of ground truth used within our pipeline. Overall, none of the permutations show a substantial difference in the quality of results, highlighting that our methodology for creating the visible masked input and target region masks is robust. However, results with any added ground truth tend to perform better than those without it. While this may seem obvious, it also reveals some failure cases in our methods and suggests a slight lack of robustness in the video diffusion model. Ground truth bounding boxes appear to have the greatest impact on mitigating these failures, as all situations where ground truth bounding boxes are used outperform their predicted counterparts. This is likely due to the difficulty of estimating amodal bounding boxes, especially when an object interacts with the environment behind an occlusion, which requires a strong semantic understanding.

## 7. Discussion

Our primary focus in this work was to develop a dataset and evaluation metrics specifically designed for assessing amodal segmentation on video, given only a single query frame and the video frames themselves. We aimed for realistic data that reflects real-world scenarios, and we believe our compositing approach successfully achieves this. This method produces videos with natural motion and accurate ground truth data, all without relying on synthetic data, human estimations, or 3D re-projection techniques. One current limitation of our dataset collection process is its dependence on a static camera setup. Future work will explore whether this constraint can be addressed by incorporating controlled camera motion, as well as building on this dataset with further examples. We also describe a pipeline which provides high level results compared to other existing methods. We hope that this framework encourages further research and development within the community, building on the techniques and findings we have established.

## References

- [1] Mihee An, Emily C Marcinowski, Lin-Ya Hsu, Jaclynn Stankus, Karl L Jancart, Michele A Lobo, Stacey C Dusing, Sarah W McCoy, James A Bovaird, Sandra Willett, et al. Object permanence and the relationship to sitting development in infants with motor delays. *Pediatric Physical Therapy*, 34(3):309–316, 2022. 1
- [2] Jiayang Ao, Qihong Ke, and Krista A Ehinger. Image amodal completion: A survey. *Computer Vision and Image Understanding*, 229:103661, 2023. 1
- [3] Max Bain, Arsha Nagrani, Gül Varol, and Andrew Zisserman. Frozen in time: A joint video and image encoder for end-to-end retrieval. In *IEEE International Conference on Computer Vision*, 2021. 3
- [4] Philipp Bergmann, Tim Meinhardt, and Laura Leal-Taixe. Tracking without bells and whistles. In *Proceedings of the IEEE/CVF international conference on computer vision*, pages 941–951, 2019. 2
- [5] Andreas Blattmann, Tim Dockhorn, Sumith Kulal, Daniel Mendelevitch, Maciej Kilian, Dominik Lorenz, Yam Levi, Zion English, Vikram Voleti, Adam Letts, et al. Stable video diffusion: Scaling latent video diffusion models to large datasets. *arXiv preprint arXiv:2311.15127*, 2023. 3
- [6] Alexey Bochkovskiy, Chien-Yao Wang, and Hong-Yuan Mark Liao. Yolov4: Optimal speed and accuracy of object detection. *arXiv preprint arXiv:2004.10934*, 2020. 4
- [7] Jasmin Breitenstein, Franz Jünger, Andreas Bär, and Tim Fingscheidt. Foundation models for amodal video instance segmentation in automated driving. *arXiv preprint arXiv:2409.14095*, 2024. 2
- [8] Bowen Cheng, Ishan Misra, Alexander G Schwing, Alexander Kirillov, and Rohit Girdhar. Masked-attention mask transformer for universal image segmentation. In *Proceedings of the IEEE/CVF conference on computer vision and pattern recognition*, pages 1290–1299, 2022. 1, 3
- [9] Terrance DeVries. Improved regularization of convolutional neural networks with cutout. *arXiv preprint arXiv:1708.04552*, 2017. 4
- [10] Kiana Ehsani, Roozbeh Mottaghi, and Ali Farhadi. Segan: Segmenting and generating the invisible. In *Proceedings of the IEEE conference on computer vision and pattern recognition*, pages 6144–6153, 2018. 4
- [11] Carsten F. Dormann, Jana M. McPherson, Miguel B. Araújo, Roger Bivand, Janine Bolliger, Gudrun Carl, Richard G. Davies, Alexandre Hirzel, Walter Jetz, W Daniel Kissling, et al. Methods to account for spatial autocorrelation in the analysis of species distributional data: a review. *Ecography*, 30(5):609–628, 2007.
- [12] Patrick Follmann, Tobias Bottger, Philipp Hartinger, Rebecca König, and Markus Ulrich. Mvtec d2s: densely segmented supermarket dataset. In *Proceedings of the European conference on computer vision (ECCV)*, pages 569–585, 2018. 4
- [13] Patrick Follmann, Rebecca König, Philipp Hartinger, Michael Klostermann, and Tobias Böttger. Learning to see the invisible: End-to-end trainable amodal instance segmentation. In *2019 IEEE Winter Conference on Applications of Computer Vision (WACV)*, pages 1328–1336. IEEE, 2019. 2, 4, 8
- [14] Jianxiong Gao, Xuelin Qian, Yikai Wang, Tianjun Xiao, Tong He, Zheng Zhang, and Yanwei Fu. Coarse-to-fine amodal segmentation with shape prior. In *Proceedings of the IEEE/CVF International Conference on Computer Vision*, pages 1262–1271, 2023. 4
- [15] Rohit Girdhar and Deva Ramanan. Cater: A diagnostic dataset for compositional actions and temporal reasoning. *arXiv preprint arXiv:1910.04744*, 2019. 4
- [16] Jonathan Ho, Tim Salimans, Alexey Gritsenko, William Chan, Mohammad Norouzi, and David J Fleet. Video diffusion models. *arXiv:2204.03458*, 2022. 3
- [17] Sebastian Höfer, Kostas Bekris, Ankur Handa, Juan Camilo Gamboa, Melissa Mozifian, Florian Golemo, Chris Atkeson, Dieter Fox, Ken Goldberg, John Leonard, et al. Sim2real in robotics and automation: Applications and challenges. *IEEE transactions on automation science and engineering*, 18(2):398–400, 2021. 4
- [18] Cheng-Yen Hsieh, Tarasha Khurana, Achal Dave, and Deva Ramanan. Tracking any object amodally. *arXiv preprint arXiv:2312.12433*, 2023. 2, 4, 8
- [19] Edward J Hu, Yelong Shen, Phillip Wallis, Zeyuan Allen-Zhu, Yuanzhi Li, Shean Wang, Lu Wang, and Weizhu Chen. Lora: Low-rank adaptation of large language models. *arXiv preprint arXiv:2106.09685*, 2021. 6
- [20] Y.-T. Hu, H.-S. Chen, K. Hui, J.-B. Huang, and A. G. Schwing. SAIL-VOS: Semantic Amodal Instance Level Video Object Segmentation – A Synthetic Dataset and Baselines. In *Proc. CVPR*, 2019. 2, 4, 8
- [21] Daniel Kahneman. *Thinking, fast and slow*. Farrar, Straus and Giroux, New York, 2011. 2
- [22] Lei Ke, Yu-Wing Tai, and Chi-Keung Tang. Deep occlusion-aware instance segmentation with overlapping bilayers. In *Proceedings of the IEEE/CVF conference on computer vision and pattern recognition*, pages 4019–4028, 2021. 2
- [23] Jyoti Kini, Fahad Shahbaz Khan, Salman Khan, and Mubarak Shah. Ct-vos: Cutout prediction and tagging for self-supervised video object segmentation. *Computer Vision and Image Understanding*, 238:103860, 2024. 3, 4
- [24] Adam Kortylewski, Ju He, Qing Liu, and Alan L Yuille. Compositional convolutional neural networks: A deep architecture with innate robustness to partial occlusion. In *Proceedings of the IEEE/CVF Conference on Computer Vision and Pattern Recognition*, pages 8940–8949, 2020. 2
- [25] Zhixuan Li, Weining Ye, Tingting Jiang, and Tiejun Huang. Gin: Generative invariant shape prior for amodal instance segmentation. *IEEE Transactions on Multimedia*, 2023. 2, 8
- [26] Zhixuan Li, Weining Ye, Juan Terven, Zachary Bennett, Ying Zheng, Tingting Jiang, and Tiejun Huang. Muva: A new large-scale benchmark for multi-view amodal instance segmentation in the shopping scenario. In *Proceedings of the IEEE/CVF International Conference on Computer Vision*, pages 23504–23513, 2023. 4
- [27] Keith Man and Javaan Chahl. A review of synthetic image data and its use in computer vision. *Journal of Imaging*, 8(11):310, 2022. 4

- [28] Rohit Mohan and Abhinav Valada. Amodal panoptic segmentation. In *Proceedings of the IEEE/CVF Conference on Computer Vision and Pattern Recognition*, pages 21023–21032, 2022. 2, 8
- [29] M Keith Moore and Andrew N Meltzoff. New findings on object permanence: A developmental difference between two types of occlusion. *British Journal of Developmental Psychology*, 17(4):623–644, 1999. 2
- [30] Bence Nanay. The importance of amodal completion in everyday perception. *i-Perception*, 9(4):2041669518788887, 2018. 1
- [31] Enhao Ning, Changshuo Wang, Huang Zhang, Xin Ning, and Prayag Tiwari. Occluded person re-identification with deep learning: a survey and perspectives. *Expert systems with applications*, 239:122419, 2024. 2
- [32] Maxime Oquab, Timothée Darcet, Théo Moutakanni, Huy Vo, Marc Szafraniec, Vasil Khalidov, Pierre Fernandez, Daniel Haziza, Francisco Massa, Alaaeldin El-Nouby, et al. Dinov2: Learning robust visual features without supervision. *arXiv preprint arXiv:2304.07193*, 2023. 1, 3
- [33] Ege Ozguroglu, Ruoshi Liu, Dídac Suró, Dian Chen, Achal Dave, Pavel Tokmakov, and Carl Vondrick. pix2gestalt: Amodal segmentation by synthesizing wholes. *Proceedings of the IEEE/CVF Conference on Computer Vision and Pattern Recognition (CVPR)*, 2024. 2, 3, 4, 5, 7, 8
- [34] Lu Qi, Li Jiang, Shu Liu, Xiaoyong Shen, and Jiaya Jia. Amodal instance segmentation with kins dataset. In *Proceedings of the IEEE/CVF Conference on Computer Vision and Pattern Recognition*, pages 3014–3023, 2019. 4
- [35] Alec Radford, Jong Wook Kim, Chris Hallacy, Aditya Ramesh, Gabriel Goh, Sandhini Agarwal, Girish Sastry, Amanda Askell, Pamela Mishkin, Jack Clark, et al. Learning transferable visual models from natural language supervision. In *International conference on machine learning*, pages 8748–8763. PMLR, 2021. 3, 8
- [36] Nikhila Ravi, Valentin Gabeur, Yuan-Ting Hu, Ronghang Hu, Chaitanya Ryali, Tengyu Ma, Haitham Khedr, Roman Rädle, Chloe Rolland, Laura Gustafson, et al. Sam 2: Segment anything in images and videos. *arXiv preprint arXiv:2408.00714*, 2024. 1, 3, 5
- [37] N Dinesh Reddy, Robert Tamburo, and Srinivasa G Narasimhan. Walt: Watch and learn 2d amodal representation from time-lapse imagery. In *Proceedings of the IEEE/CVF Conference on Computer Vision and Pattern Recognition*, pages 9356–9366, 2022. 4
- [38] Robin Rombach, Andreas Blattmann, Dominik Lorenz, Patrick Esser, and Björn Ommer. High-resolution image synthesis with latent diffusion models. In *Proceedings of the IEEE/CVF Conference on Computer Vision and Pattern Recognition (CVPR)*, pages 10684–10695, 2022. 3, 6
- [39] Olaf Ronneberger, Philipp Fischer, and Thomas Brox. U-net: Convolutional networks for biomedical image segmentation. In *Medical image computing and computer-assisted intervention—MICCAI 2015: 18th international conference, Munich, Germany, October 5-9, 2015, proceedings, part III 18*, pages 234–241. Springer, 2015. 6
- [40] Nataniel Ruiz, Yuanzhen Li, Varun Jampani, Yael Pritch, Michael Rubinstein, and Kfir Aberman. Dreambooth: Fine tuning text-to-image diffusion models for subject-driven generation. In *Proceedings of the IEEE/CVF conference on computer vision and pattern recognition*, pages 22500–22510, 2023. 3, 6
- [41] Jürgen Schmidhuber. Deep learning in neural networks: An overview. *Neural networks*, 61:85–117, 2015. 2
- [42] Aviv Shamsian, Ofri Kleinfeld, Amir Globerson, and Gal Chechik. Learning object permanence from video. In *Computer Vision—ECCV 2020: 16th European Conference, Glasgow, UK, August 23–28, 2020, Proceedings, Part XVI 16*, pages 35–50. Springer, 2020. 4
- [43] Elizabeth S Spelke, Roberta Kestenbaum, Daniel J Simons, and Debra Wein. Spatiotemporal continuity, smoothness of motion and object identity in infancy. *British journal of developmental psychology*, 13(2):113–142, 1995. 3
- [44] Roman Suvorov, Elizaveta Logacheva, Anton Mashikhin, Anastasia Remizova, Arsenii Ashukha, Aleksei Silvestrov, Naejin Kong, Harshith Goka, Kiwoong Park, and Victor Lempitsky. Resolution-robust large mask inpainting with fourier convolutions. In *Proceedings of the IEEE/CVF winter conference on applications of computer vision*, pages 2149–2159, 2022. 6
- [45] Luming Tang, Nataniel Ruiz, Qinghao Chu, Yuanzhen Li, Aleksander Holynski, David E Jacobs, Bharath Hariharan, Yael Pritch, Neal Wadhwa, Kfir Aberman, et al. RealFill: Reference-driven generation for authentic image completion. *ACM Transactions on Graphics (TOG)*, 43(4):1–12, 2024. 6, 7
- [46] Matthias Tangemann, Steffen Schneider, Julius Von Kügelgen, Francesco Locatello, Peter Gehler, Thomas Brox, Matthias Kümmerer, Matthias Bethge, and Bernhard Schölkopf. Unsupervised object learning via common fate. *arXiv preprint arXiv:2110.06562*, 2021. 4
- [47] Minh Tran, Khoa Vo, Kashu Yamazaki, Arthur Fernandes, Michael Kidd, and Ngan Le. Aisformer: Amodal instance segmentation with transformer. *arXiv preprint arXiv:2210.06323*, 2022. 2, 8
- [48] Basile Van Hoorick, Pavel Tokmakov, Simon Stent, Jie Li, and Carl Vondrick. Tracking through containers and occluders in the wild. 2023. 2, 3, 4, 5, 7
- [49] Devesh Walawalkar, Zhiqiang Shen, Zechun Liu, and Marios Savvides. Attentive cutmix: An enhanced data augmentation approach for deep learning based image classification. *arXiv preprint arXiv:2003.13048*, 2020. 4
- [50] Iris Wechsler, Alexander Wolf, Julian Shanbhag, Sigrid Leyendecker, Bjoern M Eskofier, Anne D Koelewijn, Sandro Wartzack, and Jörg Miehlung. Bridging the sim2real gap. investigating deviations between experimental motion measurements and musculoskeletal simulation results—a systematic review. *Frontiers in Bioengineering and Biotechnology*, 12:1386874, 2024. 4
- [51] Yuting Xiao, Yanyu Xu, Ziming Zhong, Weixin Luo, Jiawei Li, and Shenghua Gao. Amodal segmentation based on visible region segmentation and shape prior. In *Proceedings of the AAAI Conference on Artificial Intelligence*, pages 2995–3003, 2021. 2, 8

- [52] Lihe Yang, Bingyi Kang, Zilong Huang, Zhen Zhao, Xiaogang Xu, Jiashi Feng, and Hengshuang Zhao. Depth anything v2. *arXiv:2406.09414*, 2024. 5
- [53] Jian Yao, Yuxin Hong, Chiyu Wang, Tianjun Xiao, Tong He, Francesco Locatello, David P Wipf, Yanwei Fu, and Zheng Zhang. Self-supervised amodal video object segmentation. *Advances in Neural Information Processing Systems*, 35:6278–6291, 2022. 2, 4, 8
- [54] Guanqi Zhan, Chuanxia Zheng, Weidi Xie, and Andrew Zisserman. Amodal ground truth and completion in the wild. In *CVPR*, 2024. 2, 3, 4, 7, 8
- [55] Tianyi Zhang, Zheng Wang, Jing Huang, Mohiuddin Muhammad Tasnim, and Wei Shi. A survey of diffusion based image generation models: Issues and their solutions. *arXiv preprint arXiv:2308.13142*, 2023. 3
- [56] Yifu Zhang, Chunyu Wang, Xinggang Wang, Wenjun Zeng, and Wenyu Liu. Fairmot: On the fairness of detection and re-identification in multiple object tracking. *International journal of computer vision*, 129:3069–3087, 2021. 2
- [57] Yifu Zhang, Peize Sun, Yi Jiang, Dongdong Yu, Fucheng Weng, Zehuan Yuan, Ping Luo, Wenyu Liu, and Xinggang Wang. Bytetrack: Multi-object tracking by associating every detection box. In *European conference on computer vision*, pages 1–21. Springer, 2022. 2
- [58] Shengyu Zhao, Zhijian Liu, Ji Lin, Jun-Yan Zhu, and Song Han. Differentiable augmentation for data-efficient gan training. *Advances in neural information processing systems*, 33:7559–7570, 2020. 4
- [59] Liang Zheng, Zhi Bie, Yifan Sun, Jingdong Wang, Chi Su, Shengjin Wang, and Qi Tian. Mars: A video benchmark for large-scale person re-identification. In *Computer Vision—ECCV 2016: 14th European Conference, Amsterdam, The Netherlands, October 11–14, 2016, Proceedings, Part VI 14*, pages 868–884. Springer, 2016. 2
- [60] Hongru Zhu, Peng Tang, Jeongho Park, Soojin Park, and Alan Yuille. Robustness of object recognition under extreme occlusion in humans and computational models. *arXiv preprint arXiv:1905.04598*, 2019. 2
- [61] Yan Zhu, Yuandong Tian, Dimitris Metaxas, and Piotr Dollár. Semantic amodal segmentation. In *Proceedings of the IEEE conference on computer vision and pattern recognition*, pages 1464–1472, 2017. 4
- [62] Bojia Zi, Shihao Zhao, Xianbiao Qi, Jianan Wang, Yukai Shi, Qianyu Chen, Bin Liang, Kam-Fai Wong, and Lei Zhang. CoCoCo: Improving text-guided video inpainting for better consistency, controllability and compatibility. *ArXiv*, abs/2403.12035, 2024. 3, 6, 2

# Track Anything Behind Everything: Zero-Shot Amodal Video Object Segmentation

## Supplementary Material

### A. Further Dataset Generation Details

**Camera Setup** To capture the dataset, we used an iPhone 15 mounted on a fixed stand. The camera focus was locked on the primary object of interest to ensure consistent framing throughout the recording. Videos were shot in slow-motion mode to reduce motion blur, especially for fast-moving objects.

**Choosing Frames** To select background and foreground frames, we isolated distinct frame regions showcasing each and validated their alignment using alpha blending. This allowed us to confirm that the query object underwent realistic occlusions, ensuring the scenarios were challenging yet plausible.

**Segmenting Objects** To segment foreground and background objects, we utilised SAM2 [36] with a point-clicking approach, finding fewer clicks often yielded better results. Both image-level and video-level segmentation modes were employed, depending on the object’s consistency across frames. Through experimentation, we observed SAM2 performed best when the segmented region encompassed an area slightly larger than the target object, enabling finer feature capture and more detailed segmentation.

**Combining Monocular Depth with Segmentation** In cases where SAM2 struggles with fine details, we leverage monocular depth to refine segmentation. By calculating the average depth within the SAM2 mask, we can exclude regions with greater depth values, effectively isolating the background. This technique enhances segmentation precision, as shown in Fig. 8, enabling visibility through intricate composited elements, like the plant in this example.

#### Compositing

We use alpha compositing to overlay the foreground occluder on the background content. For each frame, this requires three frames: 1. the ‘clean plate’  $I_{cp}$  (i.e. the empty scene with neither occluder nor background object present), 2. the scene containing the background object,  $I_{bg}$ , over which we will composite the occluder and 3. the scene containing the occluder but not the background object,  $I_{fg}$ , from which we will extract the occluder alpha matte.

$I_{fg}$  can be described as an alpha blend of the clean plate image,  $I_{cp}$ , and the unknown foreground colour,  $C_{fg}$ , using the foreground alpha  $\alpha_{fg}$  given by the segmentation process above:

$$I_{fg} = (1 - \alpha_{fg}) \cdot I_{cp} + \alpha_{fg} \cdot C_{fg}. \quad (5)$$

We solve for the foreground colour (and clamp to the range  $[0, 1]$ ) using:

$$C'_{fg} = \max \left( 0, \min \left( 1, \frac{I_{fg} - (1 - \alpha_{fg}) \cdot I_{bg}}{\alpha_{fg}} \right) \right). \quad (6)$$

We can then composite the segmented foreground occluder over the scene containing the object to be occluded:

$$I_{comp} = (1 - \alpha_{fg}) \cdot I_{bg} + \alpha_{fg} \cdot C'_{fg}. \quad (7)$$

For accurate compositing, the foreground alpha should be soft to correctly handle non-binary blends at the boundary. In the case of a binary mask, the clean plate is not needed, since the foreground colour is equal to the foreground image in all pixels inside the binary foreground mask.

### B. Further Pipeline Details

Expanding on the details in Section 4, our pipeline accommodates video clips of arbitrary length despite the fine-tuned video diffusion model’s 64-frame limit. To process longer videos, we divide them into manageable chunks. Each chunk is initiated with a frame where the object is visible and non-occluded to provide a clear starting point for generation. The target clip length for these chunks is 16 frames, balancing model performance and practical constraints. However, if the video dynamics or occlusion patterns do not permit consistent 16-frame segments, chunk lengths may vary to ensure the pipeline remains adaptable while maintaining performance.

### C. Fine Tuning Implementation Details

Expanding on Section 5, Fig. 9 provides an overview of our training process. Random masks are generated and applied to input images, with areas outside the object mask being replaced by white pixels, to enforce the model’s generation of consistent white backgrounds. This ensures that the training images simulate controlled occlusions. The ticks and crosses in the diagram indicate which images contribute to the loss calculation. Non-occluded frames (ticks) are trusted since the occlusions in these images are fully artificial and therefore under our control. We provide full sequences to the model to encourage temporal consistency. We trained our model for 500 steps, using a resolution of 512x512 for input images and a learning rate of 1e-3. Due to memory constraints, the batch size was set to 1 to accommodate the full sequence of 16 frames per training iteration.

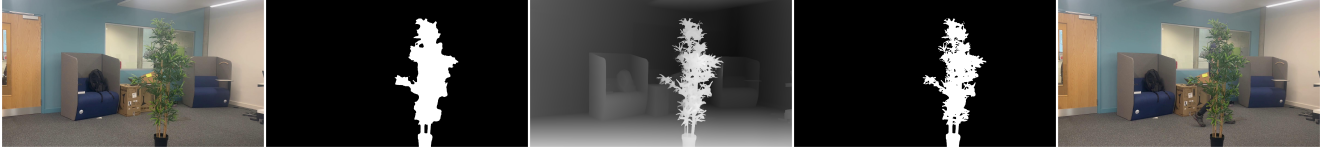


Figure 8. Showcasing how we combined SAM2 outputs with monocular depth to produce better compositions. From left to right: original frame, SAM2 output, monocular depth output, SAM2 combined with monocular depth output and finally composited frame.



Figure 9. Showcasing the video diffusion training methodology. Row 1: Original frames. Row 2: Random binary masks, Row 3: Object mask after binary mask applied, Row 4: Frames after white background and binary masks applied. Ticks represent non-occluded frames.

	Occlusion IoU	Full Occluded IoU	Non Visible Pixels IoU
Baseline COCO [62]	48.4	4.58	39.0
TABE Fine Tuned COCO	<b>65.8</b>	<b>41.8</b>	<b>48.7</b>

Table 4. Showcasing how our finetuning methodology improves results in our TABE pipeline.

Training and inference were carried out using an NVIDIA A40 GPU. Table 4 illustrates how our video specific fine-tuning greatly improves output results. The main increase is seen in the Full Occluded IoU metric. This shows our fine-tuning process allows for the model to now be able to produce better quality masks when an object is fully occluded. Other metrics reflect the baseline capabilities of the COCO model [62], showcasing its initial performance before fine-tuning.

## D. Ablation Studies

**Frame Lengths Through Inference** Fig 10 demonstrates the effect of varying the number of frames processed by the model during inference. The optimal number of frames is 16, which matches the training setup. As mentioned in B we must ensure that there is a non-occluded frame at the start of each sequence. In cases where no non-occluded frames

exist for longer sequences (greater than 16 frames), the entire sequence is treated as a single chunk. Despite the need to process longer sequences in some situations, the model handles them well, with only relatively minor performance losses. These small drops are likely due to compounding generation issues across longer sequences.

**Number of Images for Fine Tuning** As demonstrated in 11 the number of training images used for fine-tuning impacts the model’s output quality. Remarkably, the model performs respectably even with just one training example, showcasing its robustness. However, overall performance tends to improve as the number of training images increases. Interestingly, for these instances optimal results are achieved with just 10 training images. Two factors may explain this phenomenon. First, fine-tuning on a single video instance might not allow the model to reach a global optimum, with diffusion models introducing additional noise during generation. Second, larger training datasets may include images that differ significantly in pose or appearance from the target task, introducing non-optimal training data. This raises an intriguing avenue for future research: optimising the selection of training images to enhance fine-tuning outcomes systematically.

**Bounding Box Size** In Fig 12 we show how varying the

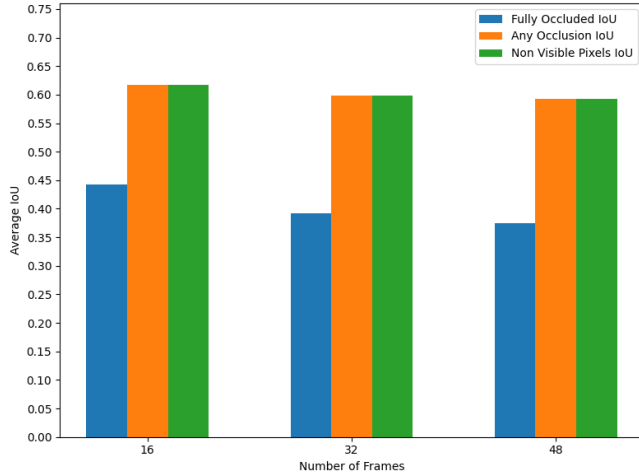


Figure 10. Illustration of how changing number of frames input to model for inference affects performance. Run on a subset of 10 different clips from TABE-51 with enough total frames to allow for this experiment.

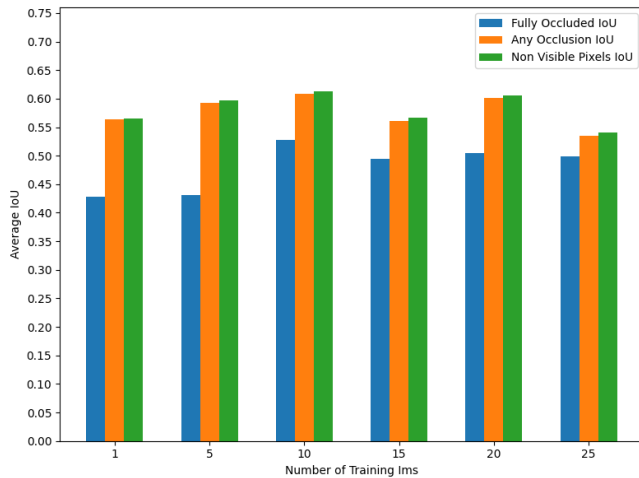


Figure 11. Evaluation of the impact of changing number of non-occluded frames the model is fine-tuned on. Run on a subset of 5 different clips from TABE-51 with enough total non-occluded frames to allow for this experiment.

size of the estimated amodal bounding box affects the overall performance of the pipeline. If we do not expand or contract the bounding box, we get optimal results for any occlusion and non visible pixel metrics. We can see that any expansion of our estimated bounding boxes causes all metrics to drop, this is as when the model is given a larger region to generate in, it is likely to generate some false positive components or overestimate the scale of the object. Contracting the bounding box causes occlusion and non visible pixel metrics to slowly start to decrease, but interestingly increases the fully occluded metric when slightly contrac-

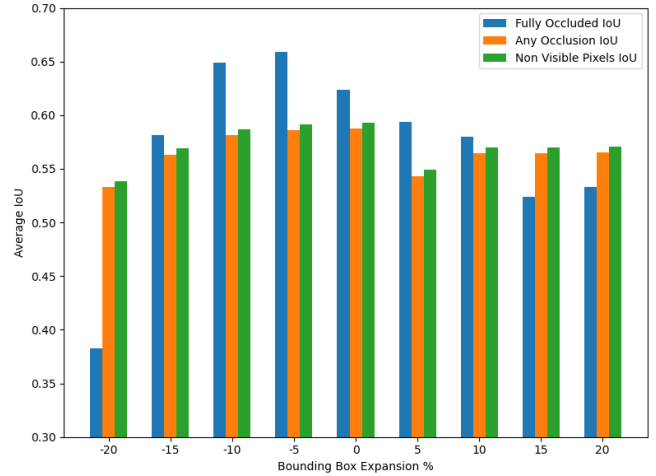


Figure 12. Evaluation of impact of expanding or contracting our estimated bounding boxes by  $X\%$ . Run on a subset of 5 different videos from TABE-51.

tion is added. Although the increase only is a maximum of a few percent, it shows that our estimated bounding box is likely slightly too large in these fully occluded regions.

## E. Qualitative Results

Fig 14 shows some further qualitative results on other public datasets, namely DAVIS <sup>1</sup> and OVIS <sup>2</sup>. Our TABE results, presented on the second row of each frame block, demonstrate superior performance across various settings when compared to competing methods—TCOW [48], Pix2Gestalt [33], and SDAmodal [54]—which are shown on the lower rows. For reference, the top row in each block displays the ground truth visible pixels.

## F. Failure Cases

**SAM2 Issue** Fig. 15 demonstrates a limitation of SAM2 [36] in tracking objects through prolonged occlusion. When the skier moves behind the hill, SAM2 cannot maintain the segmentation, failing to resume tracking once the skier reappears. The extended duration of occlusion results in no visible pixels for our pipeline to use.

**Monocular Depth Issue** This issue is less about a failure of monocular depth estimation and more about how depth information is interpreted within our pipeline and the ambiguity it can possess. Figure 16 illustrates how transparent

<sup>1</sup>Jordi Pont-Tuset, Federico Perazzi, Sergi Caelles, Pablo Arbelaez, Alex Sorkine-Hornung, and Luc Van Gool. The 2017 davis challenge on video object segmentation. arXiv preprint arXiv:1704.00675, 2017

<sup>2</sup>Jiyang Qi, Yan Gao, Yao Hu, Xinggong Wang, Xiaoyu Liu, Xiang Bai, Serge Belongie, Alan Yuille, Philip Torr, and Song Bai. Occluded video instance segmentation: A bench-mark. International Journal of Computer Vision, 2022

objects, such as windows, are handled in monocular depth maps. Although the depth measurement is technically accurate, reflecting the flat window plane, our use case demands treating the window as a fully transparent surface. For effective occlusion estimation, the depth value should correspond to the object behind the window rather than the window itself. In cases like this, the person behind the glass is assigned the depth of the window plane, resulting in an incorrect occlusion estimate.

**Bounding Box Estimation Issue** In Figure 17, we illustrate two examples in which our bounding box estimation logic fails. In the first example, the ball bounces off the solid bench in the background, whilst occluded. To accurately estimate this motion, a robust world model is needed, which our current bounding box estimation method lacks. In the second example, the bounding box estimation relies on depth information to gauge whether the object has grown smaller or shifted. Due to the perspective difference between the ground and the person, the model misinterprets the ground as occluding the person, even though it is not, leading to incorrect bounding box placement.

**Generation Issue** Figure 18 demonstrates three failures in our pipeline’s generative process. The first clip shows the model distorting the shape of the ball, which occurs because the estimated bounding box is of an incorrect shape, leading the fine-tuned video diffusion model to generate shapes based on this flawed estimation. In the second clip, the model tries to fill the space within the bounding box but ends up hallucinating additional limbs and a head. This is another case where the bounding box estimation fails, causing the model to generate unrealistic body parts. The third clip highlights a significant misestimate of the shape, again partly due to an incorrect bounding box, which results in an inaccurate object representation. These failures underline the crucial role of accurate bounding box estimation and its impact on the model’s ability to generate realistic objects.

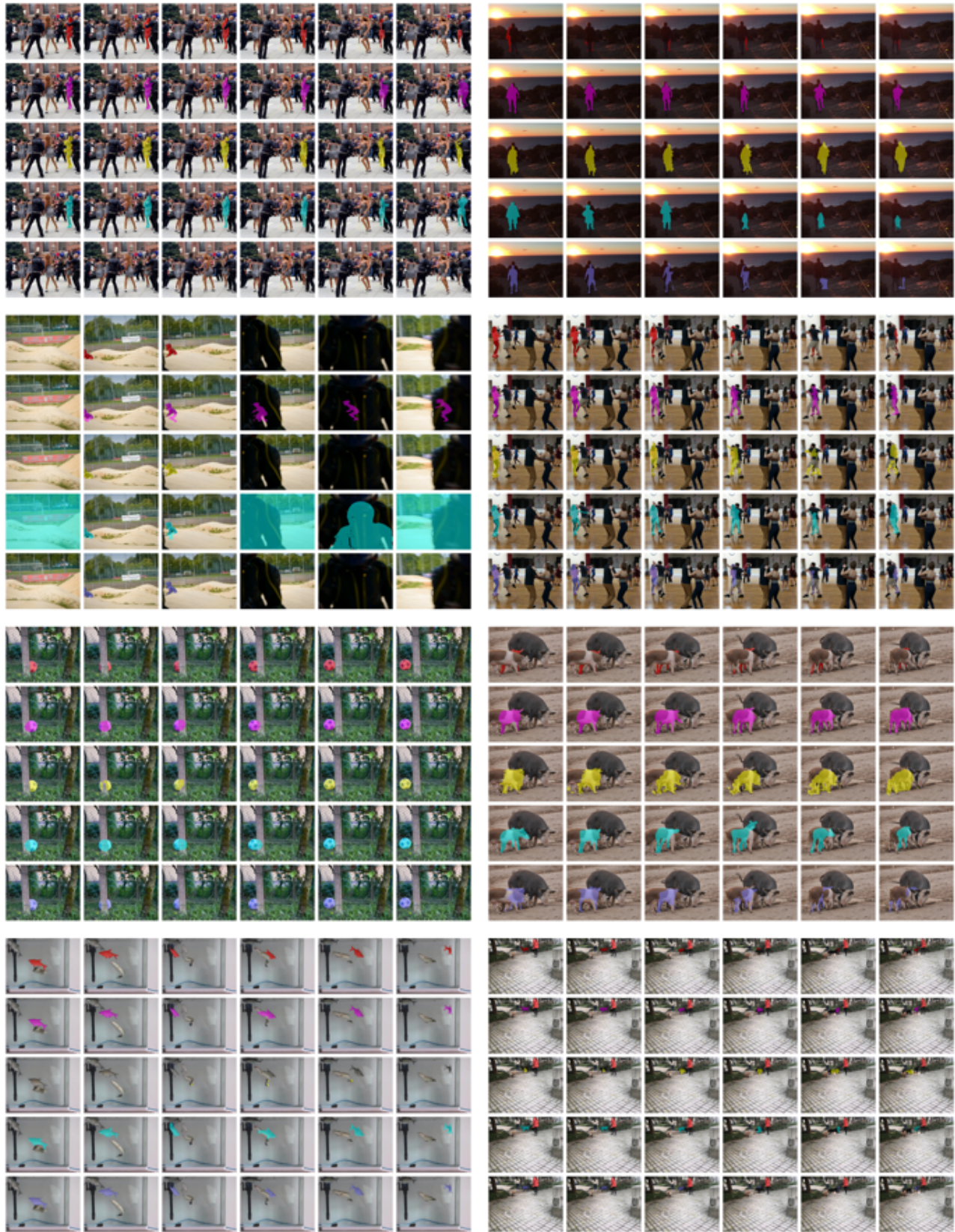


Figure 13. Qualitative results shown running DAVIS and OVIS. We show ground truth visible masks (top row: red), our TABE predictions (2nd row: magenta), TCOW predictions (3rd row: yellow), pix2gestalt predictions (4th row: sky blue) and sdmodal predictions (5th row: dark blue)

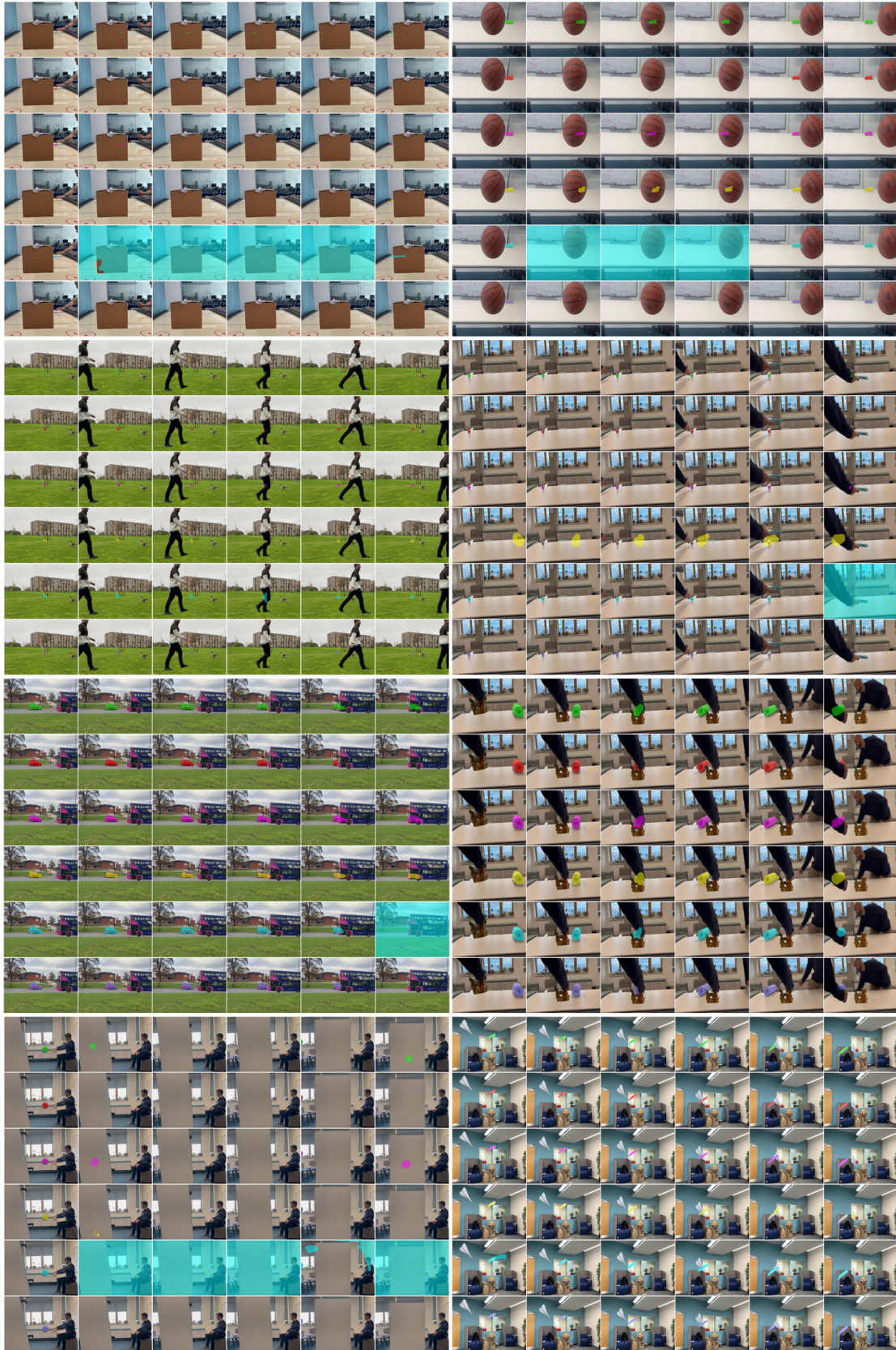


Figure 14. Qualitative results shown running TABE-51. We show ground truth amodal masks (top row: green, ground truth visible masks (2nd row: red), our TABE predictions (3rd row: magenta), TCOW predictions (4th row: yellow), pix2gestalt predictions (5th row: sky blue) and sdamodal predictions (6th row: dark blue)



Figure 15. Showcasing SAM2 failing to segment the skier after the large occlusion. Red overlay mask is the SAM2 prediction

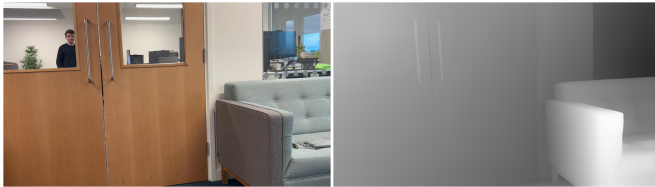


Figure 16. Illustrating how monocular depth for transparent objects doesn't provide us with usable information.



Figure 17. Failure cases of estimating bounding boxes. Red showcases the estimated bounding box while green is the ground truth.

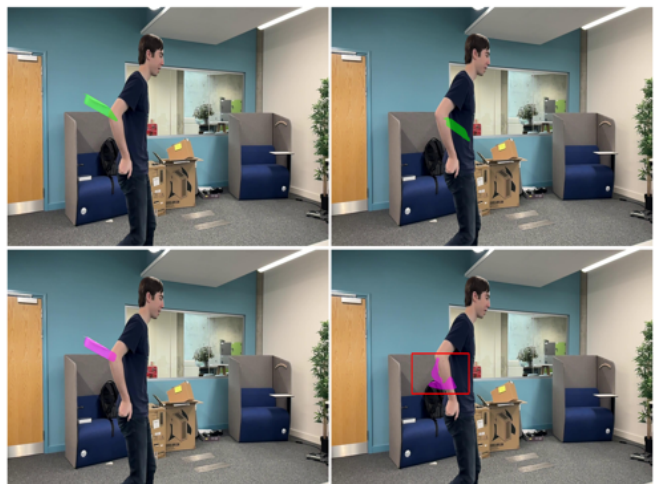
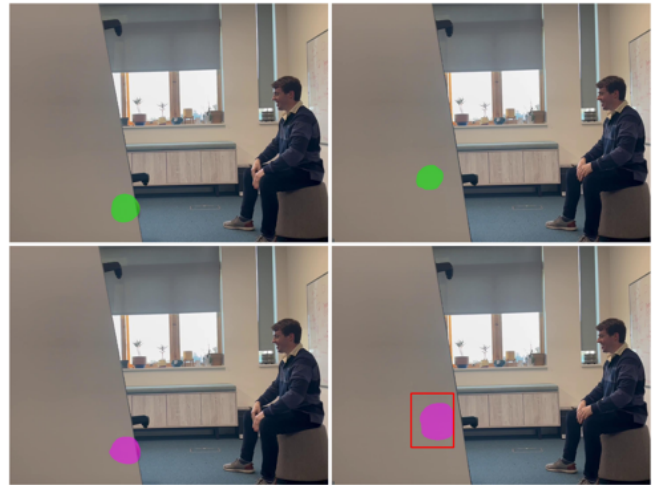


Figure 18. Failure cases of our TABE pipeline. Green represents the ground truth amodal mask, while purple is our TABE prediction. The red rectangle is our estimated bounding box.